ACS OMEGA

Open Access

http://pubs.acs.org/journal/acsodf

Article

Designed Synthesis and Electrochemical Performance Regulation of the Hierarchical Hollow Structure Cu_2S/Cu_7S_4/NC Anode for Hybrid Supercapacitors

Yu Yin, Shuo Zhang, Yaoxuan Liu, Zunyun Huang, Wenbin Sun, Mingze Zhang, Enzhen Zhou, Haihui Wu, Liu Yang,* Xiaohui Guan,* and Penggang Yin

Cite This: *ACS Omega* 2024, 9, 11883−11894

Read Online

ACCESS | Metrics & More | Article Recommendations | Supporting Information

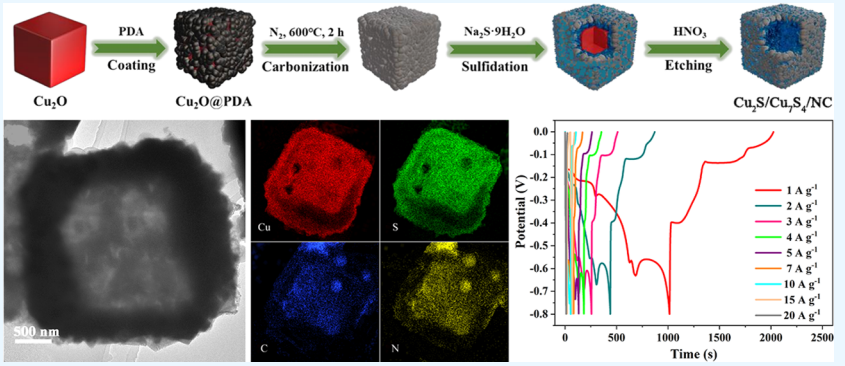

ABSTRACT: Copper-based compounds have attracted increasing attention as electrode materials for rechargeable devices, but their poor conductivity and insufficient stability inhibit their further development. Herein, an effective method has been proposed to improve the electrochemical properties of the copper-based electrodes by coating carbon materials and generating unique micro/nanostructures. The prepared Cu_2S/Cu_7S_4/NC with hierarchical hollow structure possesses excellent electrochemical performance, attributing to the composition and structure optimization. The superior charge storage performance has been assessed by theoretical and experimental research. Specifically, the Cu_2S/Cu_7S_4/NC exhibits remarkably higher electrical conductivity and lower adsorption-free energy for O* and OH* than those of Cu_2O. Moreover, the Cu_2S/Cu_7S_4/NC delivers a high specific capacitance of 1261.3 F·g^{-1} at the current density of 1 A·g^{-1} and also has great rate performance at higher current densities, which are much better than those of the Cu_2O nanocubes. In addition, the assembled hybrid supercapacitor using Cu_2S/Cu_7S_4/NC as the anode exhibits great energy density, power density, and cycling stability. This study has proposed a novel and feasible method for the synthesis of high-performance copper-based electrodes and their electrochemical performance regulation, which is of great significance for the advancement of high-quality electrode materials and rechargeable devices.

1. INTRODUCTION

With the development of urbanization and industrialization, the consumption of traditional energy sources, like coal, petroleum, and natural gas, is increasing rapidly, and problems like environmental pollution and resource shortage caused by the excessive consumption of traditional sources have become more and more serious. The advancement and utilization of new energy resources have been assumed to be one of the best solutions to protect the environment and realize sustainable development. However, the new energy resources, such as solar energy, wind energy, hydropower, tidal energy, geothermal energy, and so on, have the characteristics of intermittency and instability, which greatly limit their application and development. The energy storage and conversion devices could be employed in the new energy resource system to improve efficiency and realize large-scale applications.[1−6]

Aqueous rechargeable devices have attracted substantial attention due to their superior advantages, such as high safety, convenient operation, ideal energy and power density, low cost, and so on.[7−9] Among them, supercapacitors have been used as a new type of green energy storage device in many areas, for example, backup power systems, portable electronic devices, hybrid electric vehicles, and so on. Nevertheless, due

Received: December 2, 2023
Revised: January 19, 2024
Accepted: February 8, 2024
Published: March 1, 2024

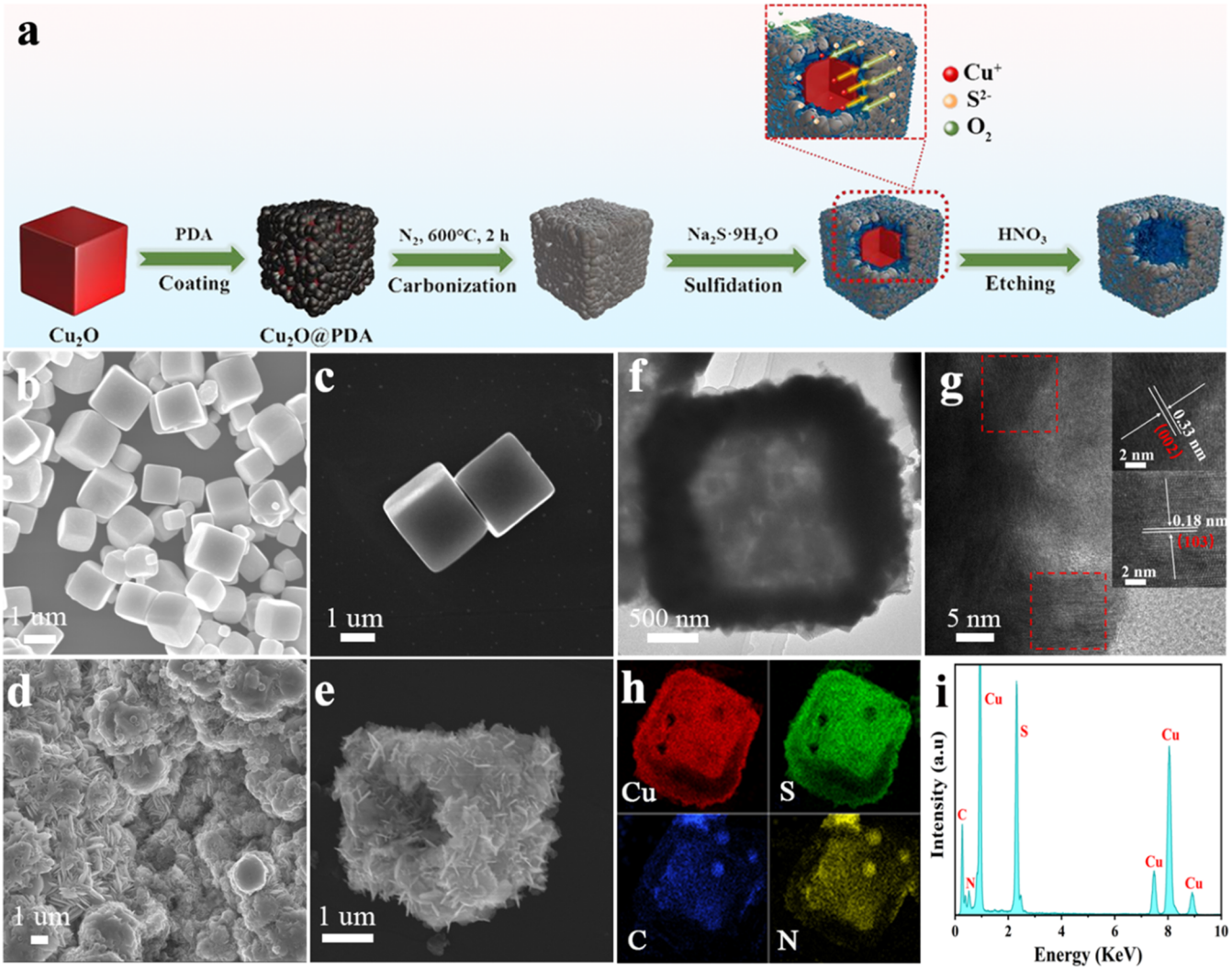

Figure 1. (a) Schematic description for the synthetic process of Cu_2S/Cu_7S_4/NC with hierarchical hollow structures. The SEM images of (b, c) Cu_2O and (d, e) Cu_2S/Cu_7S_4/NC. (f) TEM and (g) HRTEM images of Cu_2S/Cu_7S_4/NC. (h, i) The EDS and elemental mapping images of Cu_2S/Cu_7S_4/NC.

to the electrochemical energy storage process mainly occurring on the surface of the electrode, the energy density of supercapacitors is generally inferior to the batteries, which also becomes the primary challenge for the supercapacitors.[9] Therefore, the exploration of effective strategies to enhance the energy density without decreasing the power density has become the hotspot in the field of supercapacitors. Positive and negative electrodes are the main constituent parts of the supercapacitors, which have dominant effects on the electrochemical performance of the devices. Electric double-layer capacitive (EDLC)-type electrodes are one of the important kinds of materials, and the charge storage relies on the electrostatic adsorption of electrolyte ions on the interface of the electrode and electrolyte. Generally, the widely used EDLC-type electrodes, such as activated carbon, carbon nanotube, graphene, and so on, could provide relatively satisfactory cycling performance, due to their high structural stability.[10] Additionally, the battery-type electrodes storage charge by the occurrence of ions insertion/extraction or reversible redox reactions, which could provide much higher energy density. Hybrid supercapacitors (HSCs) are assembled by the electrodes with different charge storage mechanisms, which are the capacitive-type and the battery-type electrodes. Thus, hybrid supercapacitors usually could take advantage of the merits of the two types of electrodes, presenting high energy density, power density, and long-term cycling stability.

Copper-based compounds have many merits, such as abundant reserves, low price, environmental friendliness, diverse valence states, and so on. And they have great potential to be used as electrodes in aqueous rechargeable devices.[11−16] Amirtharaj and Mariappan[17] prepared interconnected CuO nanosheets, and the material delivered a high specific capacitance of 638 $F{\cdot}g^{-1}$ at the current density of 1 $A{\cdot}g^{-1}$, owing to the unique structure. Barqi et al.[18] prepared Cu_2S crystal particles, which exhibited great specific capacitance of 677 $F{\cdot}g^{-1}$ at 1 $A{\cdot}g^{-1}$. However, copper-based compounds usually suffer from poor stability and electrical conductivity, as well as irreversible side reactions during the electrochemical process, which could greatly impair the electrochemical performance of the electrodes. In order to alleviate the negative effects, it is useful to compose copper-based compounds with other materials with superior electrical conductivity and stability, which could effectively enhance the specific capacitance and cycle stability of the electro-

https://doi.org/10.1021/acsomega.3c09627
ACS Omega 2024, 9, 11883−11894

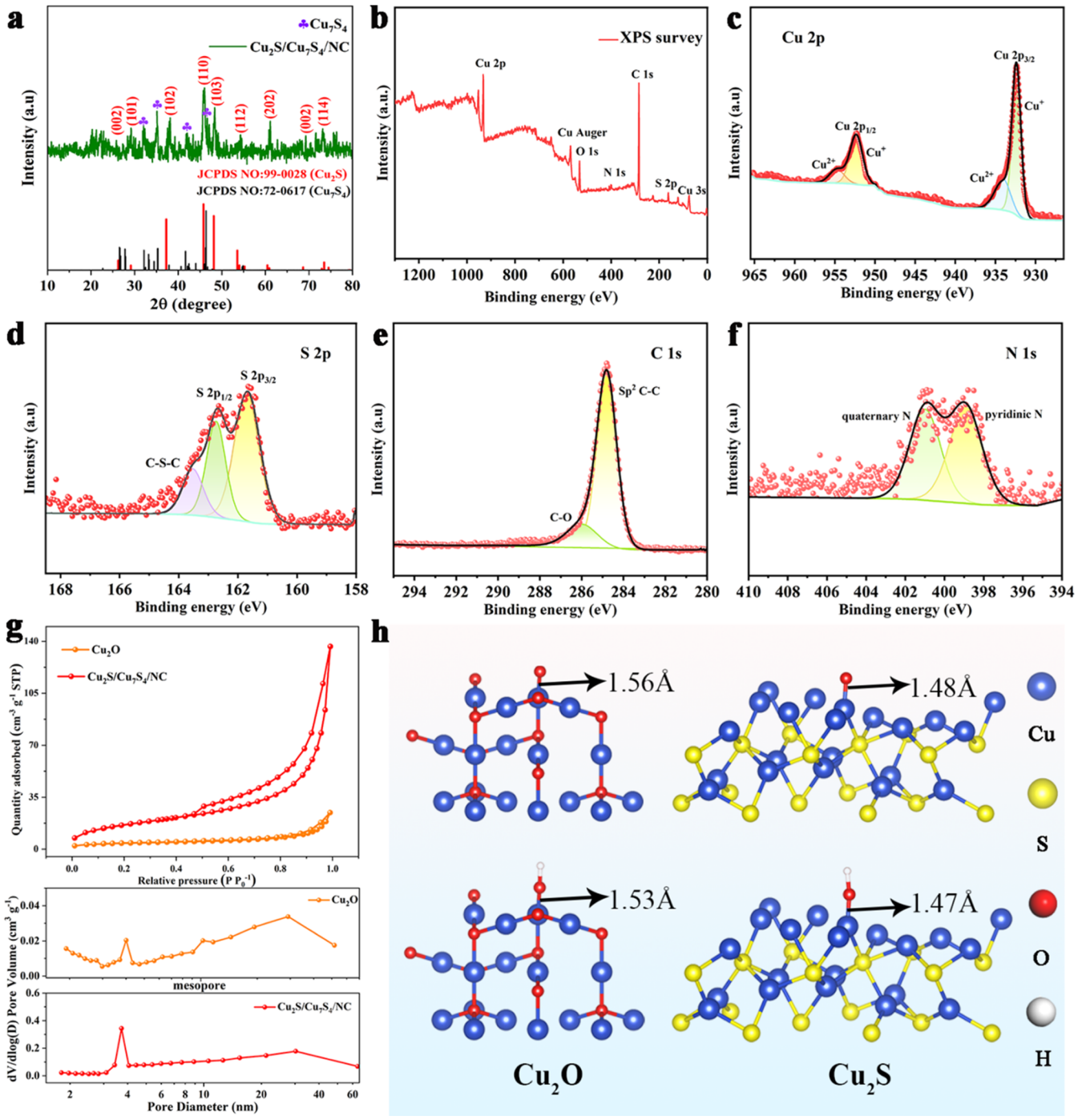

Figure 2. (a) XRD pattern of Cu_2S/Cu_7S_4/NC. The XPS spectra of Cu_2S/Cu_7S_4/NC: (b) survey spectrum; (c) Cu 2p spectrum; (d) S 2p spectrum; (e) C 1s spectrum; (f) N 1s spectrum. (g) N_2 adsorption−desorption isotherm loops and BJH pore-size distribution of Cu_2S/Cu_7S_4/NC and Cu_2O. (h) Side views for the atomic structures of Cu_2O and Cu_2S after adsorbing OH* and O* groups.

des.[19,20] Peng et al.[21] prepared CuS@PPy composites to improve the electrochemical performance of CuS. The newly generated unique structure of the composites could greatly inhibit the structure expansion during the charge and discharge procedure, and the electrode had admirable cycling stability of 88% specific capacitance retention after 1000 cycles.

In this work, nitrogen-doped carbon material has been composed with copper sulfide to regulate the stability and electrical conductivity of the copper-based compound. The structure, composition, and electrochemical performance of the prepared Cu_2S/Cu_7S_4/NC composites have been carefully characterized and studied. According to the experimental and theoretical results, the sulfidizing treatment, the coated carbon material, and the unique hierarchical hollow structure have essential effects on the electrochemical performance improvement of the anode. The sulfurized product has distinctively higher electrical conductivity and lower adsorption-free energy for the electrolyte ions than those of the Cu_2O nanocubes. Moreover, the Cu_2S/Cu_7S_4/NC delivers a high specific capacitance of 1261.3 $F{\cdot}g^{-1}$ at the current density of 1 $A{\cdot}g^{-1}$ and also has great rate performance at higher current densities, which are much better than those of Cu_2O. The Cu_2S/Cu_7S_4/

https://doi.org/10.1021/acsomega.3c09627
ACS Omega 2024, 9, 11883−11894

NC also has satisfactory application potential using as the anode in hybrid supercapacitors, which could provide great energy density, power density, and cycling stability.

2. RESULTS AND DISCUSSION

2.1. Material Synthesis and Characterization. The preparation process of the Cu_2S/Cu_7S_4/NC composites with hierarchical hollow cubic structure is shown in Figure 1a. First, the cubic Cu_2O template has been prepared by a simple chemical precipitation method. Then polydopamine (PDA) is coated on the Cu_2O nanocubes by the in situ polymerization process. However, the self-polymerization and the formation of PDA spheres are inevitable during the above process, and the appropriate modulation of the dopamine hydrochloride dosage is crucial for the uniform coating of the PDA layer. Afterward, the above product is annealed to turn the PDA coating into carbon material. Subsequently, the annealed product directly reacts with $Na_2S{\cdot}9H_2O$ at room temperature to prepare the corresponding sulfide. During this process, the dosage of $Na_2S{\cdot}9H_2O$ could greatly increase the S^{2-} ion concentration near the surface of the annealed product, leading to a larger concentration difference between the Cu^+ ions and the S^{2-} ions. Therefore, the S^{2-} ions prefer to diffuse along the concentration gradient during the reaction, reacting with Cu^+ ions on the carbon material to generate copper-based sulfide, and the hollow structure could be formed because of the Kirkendall effects.[22−27] As the gradual growth of the sulfide and the diffusion of the Cu^+ ions, the sulfide could be generated on both sides of the carbon layer. Then, the above product is etched by aerobic acid to eliminate the residue impurities. The Cu^+ in the material could be inevitably partially oxidized to high valence states. Finally, the Cu_2S/Cu_7S_4/NC composites with hierarchical hollow structures could be obtained.

Scanning electron microscope (SEM) characterization has been used to study the structure and morphology of the Cu_2O and Cu_2S/Cu_7S_4/NC composites and also to analyze the influences of material synthetic conditions on their morphologies. As shown in Figure 1b,c, the Cu_2O template exhibits a regular cubic structure with a smooth surface, and no other impurities could be found. The unique and uniform structure of Cu_2O makes it an excellent candidate as the template and precursor to regulate the morphology and structure of the final products. As shown in Figure 1d,e, the Cu_2S/Cu_7S_4/NC composites present the basic cubic structure as the templates. However, the cubic structure shell is composed of sheet-like nanostructures, which could be observed on both the internal and external sides of the material. Moreover, from the broken structure, it is clear that Cu_2S/Cu_7S_4/NC has a hollow structure. The formation of the unique structure, on the one hand, is due to the uniform coating of a dense carbon layer on the surface of the Cu_2O template, which could stabilize the cubic structure after the following treatments. On the other hand, because of the concentration and diffusion rate differences of the S^{2-} ions and Cu^+ ions, according to the Kirkendall effect,[22−27] the consumption rate of Cu_2O core is higher than the growth rate of copper sulfide shell, which is beneficial for the generation of hollow structures.

Transmission electron microscopy (TEM) analysis has been used to further confirm the microstructure of the Cu_2S/Cu_7S_4/NC composites. As shown in Figure 1f, the Cu_2S/Cu_7S_4/NC composites possess hollow cubic structures, and some sheet-like nanostructures could also be clearly recognized. The unique structure composed of the carbon shell and the lamellar structure enables more exposed active sites to directly contact with the electrolyte ions, which could improve the electrochemical activity of the material. The TEM analysis is in agreement with the SEM results. As shown in Figure 1g, the high-resolution TEM (HRTEM) image shows two obvious lattice stripes with the spacing of 0.33 and 0.18 nm, respectively, which could be completely indexed to the (002) and (103) crystal facets of Cu_2S (JCPDS NO: 99−0028). The analysis is consistent with the X-ray diffraction (XRD) result. The elemental composition and distribution of the Cu_2S/Cu_7S_4/NC composites are analyzed by the energy-dispersive spectrometer (EDS) characterization, and the results are shown in Figure 1h,i. It is evident that the Cu_2S/Cu_7S_4/NC is mainly composed of four elements, Cu, S, C, and N elements. The Cu, S, C, and N elements are evenly distributed in the cubic structure of Cu_2S/Cu_7S_4/NC.

The composition and crystalline structure of the Cu_2S/Cu_7S_4/NC composites are analyzed by XRD characterization. As shown in Figure 2a, the main diffraction peaks fit well with the Cu_2S standard card (JCPDS NO: 99−0028), and the peaks at 26.2, 29.1, 37.2, 45.8, 48.1, 53.5, 60.4, and 73.4° correspond to the (002), (101), (102), (110), (103), (112), (202), and (114) crystal faces of Cu_2S. In addition, several obvious characteristic peaks of Cu_7S_4 could also be observed in the XRD spectrum, which fit well with the standard card of Cu_7S_4 (JCPDS NO: 72−0617). The formation of Cu_7S_4 could be attributed to the partial oxidization of Cu^+ during the synthetic process. The XRD pattern for Cu_2O is shown in Figure S1, and it can be seen that the characteristic peaks of Cu_2O are sharp and consistent with the standard card, demonstrating the successful preparation of Cu_2O with no impurities.

The chemical composition and valence state of the Cu_2S/Cu_7S_4/NC composites are confirmed by the X-ray photoelectron spectroscopy (XPS) characterization. As shown in Figure 2b, the XPS survey spectrum shows the obvious characteristic peaks for the elements of Cu, S, C, and N, which further verifies the constituent elements of the composites. As shown in Figure 2c, the high-resolution XPS spectrum of Cu 2p presents two major peaks corresponding to the Cu $2p_{3/2}$ and Cu $2p_{1/2}$. The fitted peaks centered at 932.45 and 952.35 eV correspond to the binding energies of Cu^+.[28,29] Those two peaks have a larger integrated area, which indicates that the Cu element is mainly in the valence state of +1. In addition, the two fitted peaks at the binding energies of 933.85 and 954.55 eV could be attributed to the existence of the copper elements with higher valence states.[30] As shown in Figure 2d, the high-resolution XPS spectrum of S 2p could be fitted into three peaks. The S $2p_{3/2}$ peak is located at 161.65 eV, and the S $2p_{1/2}$ peak is at about 162.7 eV. The peaks indicate that the main form of sulfur element in the composites is S^{2-}.[31,32] The peak centered at about 163.5 eV could be attributed to the C−S−C bonds. As shown in Figure 2e, the C 1s spectrum could be fitted into two peaks at 284.8 and 286.0 eV, corresponding to the sp^2 C−C and C−O bonds.[33,34] As shown in Figure 2f, the high-resolution XPS spectrum of N 1s could be fitted into two peaks. The peak at 398.8 eV indicates the pyridine nitrogen, and the peak at 401.0 eV represents the quaternary nitrogen. The doping of heteroatoms has been proved to be of great significance for promoting electron transport and improving electrical conductivity.[35−38] The XPS results are coincident with the abovementioned characterizations and could further confirm the composition of the product. Combined with the

https://doi.org/10.1021/acsomega.3c09627
ACS Omega 2024, 9, 11883−11894

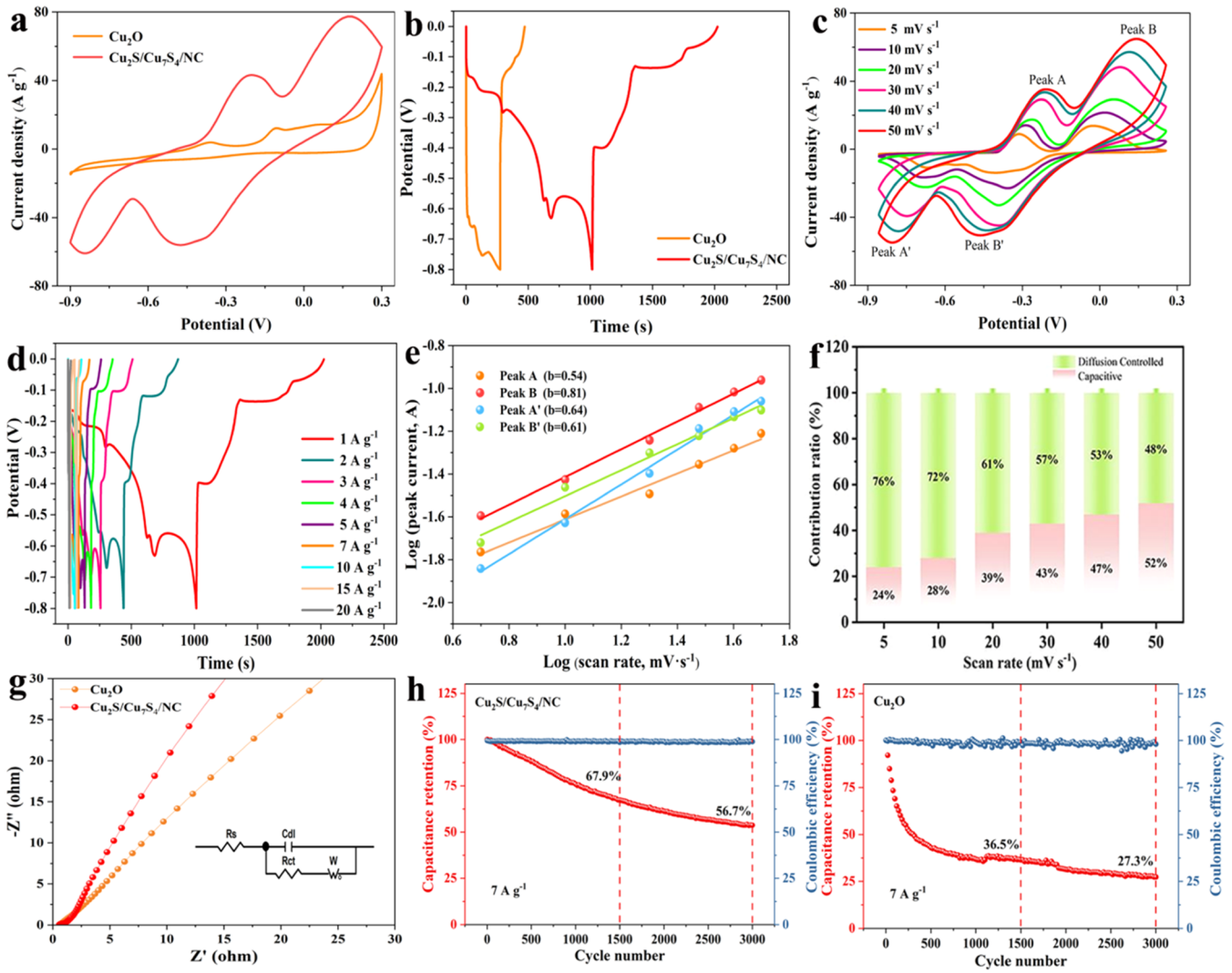

Figure 3. (a, b) CV and GCD curves of Cu_2S/Cu_7S_4/NC and Cu_2O. (c) The CV curves of Cu_2S/Cu_7S_4/NC at different scan rates. (d) The GCD curves of Cu_2S/Cu_7S_4/NC at different current densities. (e) The linear relation between CV anodic/cathodic peak currents and scan rates for Cu_2S/Cu_7S_4/NC. (f) The calculated capacitive-controlled contribution of Cu_2S/Cu_7S_4/NC during the charge storage process. (g) The EIS results of Cu_2S/Cu_7S_4/NC and Cu_2O. (h) The cycling stability of Cu_2S/Cu_7S_4/NC. (i) The cycling stability of Cu_2O.

above characterization results, the composition and structure of the prepared Cu_2S/Cu_7S_4/NC could be well verified.

The N_2 adsorption−desorption isotherms and BJH pore-size distribution of Cu_2S/Cu_7S_4/NC and Cu_2O are shown in Figure 3g. The Cu_2S/Cu_7S_4/NC has a larger Brunauer−Emmett−Teller (BET) specific surface area than that of Cu_2O. The specific surface areas of Cu_2S/Cu_7S_4/NC and Cu_2O are 60.0 and 13.7 $m^2 \cdot g^{-1}$. Moreover, Cu_2S/Cu_7S_4/NC exhibits a typical mesoporous feature, which is beneficial for electrolyte ion transportation and charge storage. In this work, the charge storage performance of the anode and the hybrid supercapacitor is assessed in the alkaline electrolyte. Therefore, the adsorption ability of the main electrolyte ions has been calculated. Because Cu_2S is the main composition of the Cu_2S/Cu_7S_4/NC composites, the adsorption properties of Cu_2O and Cu_2S for OH* and O* have been studied. The atomic structures of Cu_2O and Cu_2S are shown in Figure S2. As shown in Figure 2h, the length of the Cu−OH and Cu−O bonds on Cu_2S are much shorter than those on Cu_2O, indicating that Cu_2S has much higher affinity for the electrolyte ions, which is significant for the improvement of the charge storage performance.

The coating content of the carbon material has been adjusted by the regulation of the content of PDA. During the synthetic process, the dosages of dopamine hydrochloride have been set as 50, 70, 90, 110, 130, and 150 mg. As shown in Figure S3a,b, as the dosages of dopamine hydrochloride are lower, the amounts of the coated PDA on the surface of Cu_2O are small. With the increase of the dopamine hydrochloride dosage, the self-polymerization of PDA becomes evident, and more PDA nanospheres are generated and attached to Cu_2O. At the same time, Cu_2O experiences slight dissolution, and the cubic structure dents a little. As shown in Figure S3c−f, as much more dopamine hydrochloride is added to the reaction system, the structure of the precursor obviously changes, and more PDA spheres aggregate on or off the Cu_2O nanocubes. Because the content of the carbon material has great influences on the electrochemical performance, the optimal dopamine hydrochloride dosage has been further confirmed by the following electrochemical tests.

https://doi.org/10.1021/acsomega.3c09627
ACS Omega 2024, 9, 11883−11894

The above-prepared Cu_2O with PDA-coated products have been annealed, and the SEM images of the annealed products are shown in Figure S4. As shown in Figure S4a,b, when the content of the coated PDA is lower, it is difficult to form a stable carbon protective layer outside Cu_2O, and the annealed products exhibit slight structure collapse. As shown in Figure S4c,d, as the content of PDA increases, the generated carbon layer is thicker and more stable, which could be uniformly coated on the surface of Cu_2O. The intimate contact between the materials could improve the structural stability as well as the electrochemical performance. As shown in Figure S4e,f, as the dosage of dopamine hydrochloride is much higher, the self-polymerization of PDA becomes severe, and the PDA spheres aggregate after the annealing treatment, leading to the generation of irregular structures. Thus, the optimal dopamine hydrochloride dosages could be initially confirmed to be 90 mg and 110 mg.

The dosages of $Na_2S{\cdot}9H_2O$ have been regulated, and the SEM images of the products prepared with different dosages are shown in Figure S5. When the dosage of $Na_2S{\cdot}9H_2O$ is relatively low, the vulcanization degree is limited. Moreover, with the increase of the S^{2-} ion content, much more sheet-like structures could be generated on the cubic structures, creating more active sites for charge storage. According to the SEM images, the optimal dosage could be initially set as 50 mg.

2.2. Electrochemical Performance of the Cu_2S/Cu_7S_4/NC Anode. The electrochemical performance of the as-prepared materials has been studied in a traditional three-electrode system. And the potential of the Cu_2S/Cu_7S_4/NC as an anode for hybrid supercapacitors and the charge storage mechanism have also been assessed. The cyclic voltammetry (CV) curve comparisons of Cu_2O and Cu_2S/Cu_7S_4/NC are shown in Figure 3a. It is obvious that the CV curve of Cu_2S/Cu_7S_4/NC is of larger integrated area than that of Cu_2O, which demonstrates that the Cu_2S/Cu_7S_4/NC has distinctly higher specific capacitance. As shown in Figure 3b, the galvanostatic charge−discharge (GCD) curve of Cu_2S/Cu_7S_4/NC presents a longer discharging time than that of Cu_2O, also suggesting the higher capacitance of the Cu_2S/Cu_7S_4/NC. The greatly improved electrochemical performance could be attributed to the sulfurizing treatment and the coating of carbon materials, which could improve the electrical conductivity and the electrochemical activity of the composites. Moreover, the hierarchical hollow structure could also facilitate the transportation of the electrolyte ions and provide abundant active sites, which are essential for the occurrence of the redox reactions. The CV curves of the Cu_2S/Cu_7S_4/NC obtained at different scan rates are shown in Figure 3c. It is clear that the curves are all with obvious redox peaks, indicating that the prepared sulfide electrode is battery-type. With the gradual increase of the scan rate, the shape of the CV curves has no obvious changes, indicating the great electrochemical reversibility of the electrode. But the redox peaks experience positive and negative shifts due to the polarization effect. The GCD curves of the Cu_2S/Cu_7S_4/NC tested at different current densities are shown in Figure 3d. The GCD curves are of similar charging and discharging times, preliminarily indicating the great Coulombic efficiency of the electrode. Moreover, the obvious platforms could be observed on the GCD curves, which also demonstrate the battery-type charge storage mechanism of the electrode. The analysis is in good agreement with the CV results. The specific capacitance of the Cu_2S/Cu_7S_4/NC is up to 1261.3 $F{\cdot}g^{-1}$ at the current density of 1 $A{\cdot}g^{-1}$. When the current density increases from 1 to 10 $A{\cdot}g^{-1}$, the specific capacitance of the Cu_2S/Cu_7S_4/NC composites is 637.5 $F{\cdot}g^{-1}$, corresponding to a capacitance retention rate of 50.5%. The results reveal that the prepared Cu_2S/Cu_7S_4/NC exhibits satisfactory rate performance.

To study the electrochemical reaction kinetics and the charge storage mechanism of the electrodes, the contributions of the capacitive-controlled and the diffusion-controlled process are evaluated according to the following equations[39,4039,40]

$$i_p = av^b \tag{1}$$

$$\log i_p = b \log v + \log a \tag{2}$$

$$i(v) = k_1 v + k_2 v^{1/2} \tag{3}$$

where i_p is the peak current (A), v is the scan rate ($mV{\cdot}s^{-1}$), a is a constant, b could represent the general electrochemical reaction kinetics, and k_1v and $k_2v^{1/2}$ indicate the capacitive-controlled and the diffusion-controlled contribution, respectively. If the b value is about 0.5, it indicates the diffusion-controlled process. If the b value is about 1, it means the capacitive-controlled process. As shown in Figure 3e, the b values are about 0.5, 0.6, and 0.8, which demonstrates that the charge storage mechanism of the Cu_2S/Cu_7S_4/NC is mainly the diffusion-controlled behavior, suggesting the battery-type features. Moreover, during the charge storage process, there is also a capacitive-controlled contribution. Generally, the diffusion-controlled behavior could provide high capacitance, and the capacitive-controlled behavior could promote the rate performance. Thus, the combination of the two different mechanisms could remarkably enhance the charge storage capability of the electrode. As shown in Figure 3f, the diffusion-controlled process contributes to a large proportion. With the increase of the scan rate, the proportion of diffusion-controlled behavior gradually decreases, which is mainly because of the polarization effect during the rapid charge and discharge process. The results also suggest the combination of the battery-type and capacitive charge storage mechanisms.

Electrochemical impedance spectroscopy (EIS) measurements are performed with the frequency range of 0.01−100 kHz and the amplitude of 5 mV, to further investigate the electrochemical properties of Cu_2S/Cu_7S_4/NC and Cu_2O. According to Figure 3g, the Nyquist plots of Cu_2S/Cu_7S_4/NC and Cu_2O have semicircles in the high-frequency region and approximately straight lines in the low-frequency region. In the high-frequency region, the equivalent series resistance (R_s) is numerically equal to the intercept of the x-axis, mainly including the interface resistance, the intrinsic resistance of the electrode material, and the electrolyte ionic resistance.[41] The R_s values of Cu_2S/Cu_7S_4/NC and Cu_2O are 0.57 and 0.73 Ω, and the lower R_s value of Cu_2S/Cu_7S_4/NC indicates that the material has small intrinsic resistance and interface contact resistance. According to the positive correlation between the semicircle diameter in the high-frequency region and the charge transfer resistance (R_{ct}), it could be found that the R_{ct} value of Cu_2S/Cu_7S_4/NC is much smaller than that of Cu_2O, which are 0.12 and 1.02 Ω.[42] The slope in the low-frequency region is inversely proportional to the Warburg impedance (W_z) and represents the migration resistance of the electrolyte ions in the active species.[43] The slope of the linear part of Cu_2S/Cu_7S_4/NC is obviously larger, indicating the much lower migration resistance of the electrolyte ions.

https://doi.org/10.1021/acsomega.3c09627
ACS Omega 2024, 9, 11883−11894

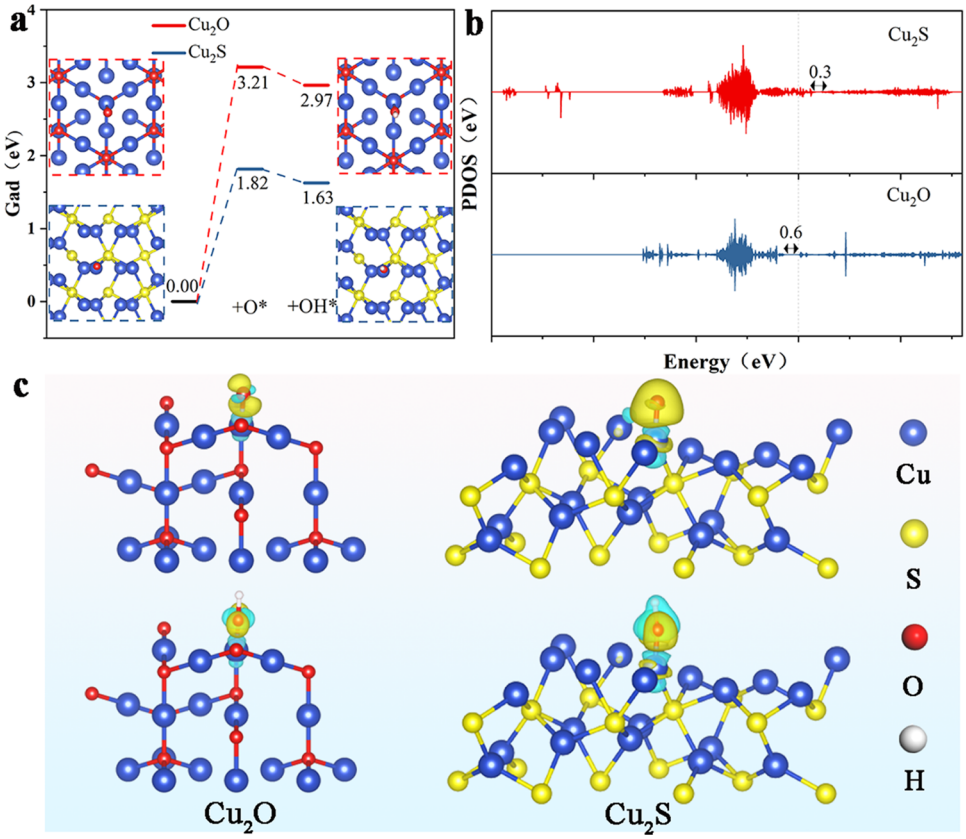

Figure 4. (a) Adsorption ability for OH* and O* of Cu_2O and Cu_2S. (b) PDOS diagrams of Cu_2O and Cu_2S. (c) Differential charge density maps of Cu_2O and Cu_2S.

The cycling stability of the synthesized Cu_2S/Cu_7S_4/NC and Cu_2O has been evaluated by performing the GCD test at 7 $A{\cdot}g^{-1}$ for 3000 cycles. As shown in Figure 3h,i, the specific capacitance of Cu_2S/Cu_7S_4/NC could be retained at 56.7% after 3000 cycles. In the whole cycling stability test, the capacitance shows a relatively slow decline process, and there is no sudden drop phenomenon. As compared with the result of Cu_2O, the specific capacitance drops rapidly at the initial stage, and the retention rate is quite lower (27.3% after 3000 cycles). Moreover, the Coulombic efficiencies of the two electrodes are about 100% during the whole cycling process. The higher electrical conductivity and cycling stability of the Cu_2S/Cu_7S_4/NC could be mainly attributed to the sulfide composition and the introduction of nitrogen-doped carbon material.

According to the experimental results, Cu_2S/Cu_7S_4/NC possesses much higher electrochemical performance than that of the Cu_2O naoncubes. Therefore, theoretical analysis has been conducted to further reveal and confirm the high electrochemical activity of the sulfurized product, and the results are shown in Figure 4. The adsorption energies for OH* and O* on Cu_2O and Cu_2S are first calculated, and the results are shown in Figure 4a. Obviously, Cu_2S has the lower adsorption energies for both of OH* and O* (1.63 and 1.82 eV) than those of Cu_2O (2.97 and 3.21 eV). The higher affinity for the electrolyte ions could be one of the main reasons for the high electrochemical performance of the sulfurized anode.

Additionally, the partial density of states (PDOS) for Cu_2O and Cu_2S are shown in Figure 4b. Compared with Cu_2O, Cu_2S presents an increased density of states over the Fermi energy level and more empty states near the Fermi level, indicating the higher electrical conductivity of Cu_2S. The atomic structure and PDOS diagram of Cu_2S/Cu_7S_4/NC are shown in Figure S6. The PDOS diagram has a peak at Fermi energy, which demonstrates much higher electrical conductivity than that of Cu_2S. The three-dimensional charge density differences of Cu_2O and Cu_2S have been calculated. As shown in Figure 4c, the yellow area means the charge accumulation and the blue area means the charge consumption. It is clear that the charge density around Cu_2S is much larger than that around Cu_2O, which indicates that the charge transport around Cu_2S is more active. The theoretical results have well illustrated that the sulfurized product exhibits higher adsorption affinity for electrolyte ions and electrical conductivity, which could dramatically facilitate the charge storage process.

The vulcanization treatment is essential for the improvement of the electrochemical performance. Thus, the dosages of $Na_2S{\cdot}9H_2O$ have been regulated as 25, 50, 75, and 100 mg, respectively. As shown in Figure S7a, the CV curves of the products at 50 $mV{\cdot}s^{-1}$ all have evident oxidation/reduction peaks, implying the occurrence of the reversible redox reactions during the energy storage process and the battery-type charge storage mechanism of the products. Among them, the product prepared with $Na_2S{\cdot}9H_2O$ dosage of 50 mg exhibits the largest CV integrated area, representing the highest specific capacitance. As shown in Figure S7b, all of the GCD curves possess obvious charging−discharging platforms, indicating a similar charge storage mechanism. Moreover, the product prepared with the dosage of 50 mg has the longest discharging time, suggesting superior charge storage capability. Therefore, the optimal dosage of $Na_2S{\cdot}9H_2O$ is determined to be 50 mg.

https://doi.org/10.1021/acsomega.3c09627
ACS Omega 2024, 9, 11883−11894

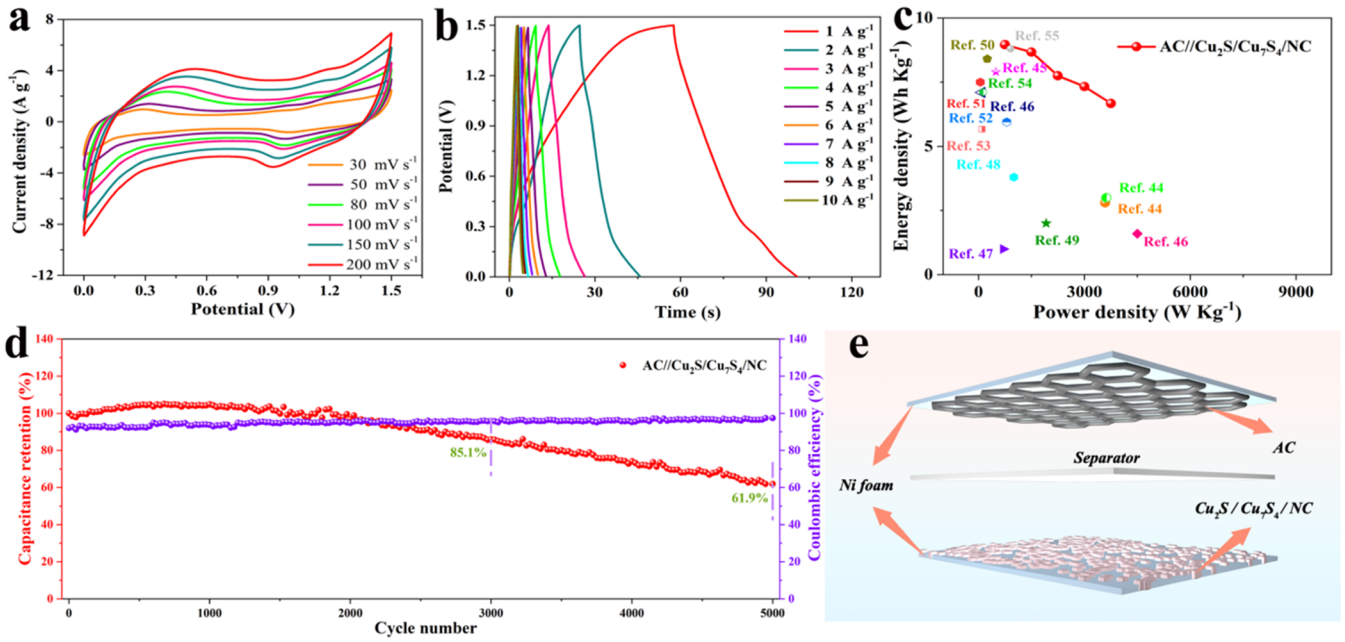

Figure 5. (a, b) CV and GCD curves of the hybrid supercapacitor tested in the voltage range of 0−1.5 V. (c) The Ragone plot of the hybrid supercapacitor. (d) The cycling stability of the hybrid supercapacitor. (e) The schematic description of the assembled hybrid supercapacitor.

2.3. Electrochemical Performance of the Hybrid Supercapacitor. The prepared Cu_2S/Cu_7S_4/NC has been used as the anode to assemble a hybrid supercapacitor with activated carbon (AC) as the cathode and 6 M KOH solution as the electrolyte. The hybrid supercapacitor was assembled to further analyze the application potential of the anode in the field of energy storage. The CV and GCD tests are applied to investigate the charge storage capability of the assembled device. As shown in Figure 5a, the CV curves obtained in the voltage range of 0−1.5 V are of basic rectangular shape, but with redox peaks, which suggests the combination of the typical electric double-layer capacitive and battery-type charge storage behavior. The capacitive behavior might be mainly attributed to the contribution of the carbon cathode, and the battery-type behavior might be mainly ascribed to the contribution of the sulfide anode. With the increase of the scan rate, the shape of the CV curves experiences nearly no change, demonstrating the great electrochemical reversibility of the device. As shown in Figure 5b, the GCD curves obtained in the voltage range of 0−1.5 V exhibit admirable Coulombic efficiencies at lower and higher current densities, which are 73.8 and 94.6% at 1 and 10 $A{\cdot}g^{-1}$. It could be calculated that the specific capacitance is 28.7 $F{\cdot}g^{-1}$ at the current density of 1 $A{\cdot}g^{-1}$, which could retain 74.3% at 5 $A{\cdot}g^{-1}$ and 60.4% at 10 $A{\cdot}g^{-1}$. As shown in Figure 5c, the energy density and power density of the device have been calculated. When the power densities are 750 and 3750 $W{\cdot}kg^{-1}$, the energy densities are 8.96 and 6.67 $Wh{\cdot}kg^{-1}$. The assembled hybrid supercapacitor also has superior energy and power densities compared with other related rechargeable devices.[44−55] The cycling stability of the supercapacitor has been evaluated and the results are shown in Figure 5d. After 3000 and 5000 cycles, the capacitance retention rates are 85.1 and 61.9%, which indicates the high cycling stability of the device. Moreover, the Coulombic efficiency is about 92% at the initial stage and could increase close to 100% afterward. The schematic description of the assembled hybrid supercapacitor is shown in Figure 5e.

3. CONCLUSIONS

In conclusion, this work has proposed a novel and feasible method to prepare a high-performance copper-based compound anode. Cu_2O with a regular cubic structure has been employed as the template, and sulfurizing treatment and carbon coating also have been applied to improve the electrochemical performance. Moreover, the unique hierarchical hollow structure could be formed during the material synthetic process. Appropriate characterizations have been conducted and well analyzed. Benefiting from the composition and structure optimization, the prepared Cu_2S/Cu_7S_4/NC possesses superior charge storage capability, such as specific capacitance, rate performance, and cycling stability, especially compared with the Cu_2O precursor. According to the theoretical and experimental results, the Cu_2S/Cu_7S_4/NC exhibits remarkably higher electrical conductivity and lower adsorption-free energy for O* and OH* than those of Cu_2O. Additionally, the Cu_2S/Cu_7S_4/NC delivers a high specific capacitance of 1261.3 $F{\cdot}g^{-1}$ at the current density of 1 $A{\cdot}g^{-1}$. In addition, the assembled hybrid supercapacitor using Cu_2S/Cu_7S_4/NC as the anode exhibits great energy density, power density, and cycling stability. The energy density could reach to 8.96 $Wh{\cdot}kg^{-1}$ at the power density of 750 $W{\cdot}kg^{-1}$, and the specific capacitance could retain 85.1% after 3000 cycles. This study has provided a novel strategy to design and synthesize satisfactory copper-based anode and also to optimize the electrochemical performance.

4. EXPERIMENTAL SECTION

4.1. Materials. All of the chemicals were of analytical grade and used without any further purification. The water used in this study was ultrapure water.

4.2. Synthesis of the Cu_2S/Cu_7S_4/NC. *4.2.1.. Synthesis of the Template.* The Cu_2O template with stable and uniform cubic structures was synthesized by the typical chemical precipitation method.[56] First, copper pentahydrate sulfate ($CuSO_4{\cdot}5H_2O$, 1.5 mmol) and trisodium citrate ($C_6H_5Na_3O_7$,

https://doi.org/10.1021/acsomega.3c09627
ACS Omega 2024, 9, 11883−11894

0.5 mmol) were dissolved in 80 mL of ultrapure water. Then, 20 mL of sodium hydroxide solution (NaOH, 1.25 M) was added during the stirring process. After 15 min, 50 mL of 0.03 M ascorbic acid solution was added dropwise under stirring. The resulting mixed solution was then aged for 1 h at room temperature. Finally, the red precipitate was collected by centrifugation, washed several times with water and ethanol, and dried at 50 °C for 12 h.

4.2.2.. Synthesis of the Cu_2S/Cu_7S_4/NC Composites. The cubic structure Cu_2O was used as the template. First, the Cu_2O template (80 mg) was evenly dispersed in 100 mL of ultrapure water. Then, trihydroxymethylthane (Tris, 0.1214 g) and dopamine hydrochloride ($C_8H_{12}ClNO_2$, 0.1100 g) were added into the above solution under stirring. The reaction was maintained for 4 h at room temperature, and polydopamine (PDA) could be formed outside the Cu_2O nanocubes. Finally, the precipitate was collected by centrifugation, washed several times with water and ethanol, and dried at 50 °C for 12 h. The above product was further annealed at 600 °C for 2 h in a nitrogen atmosphere, and PDA could be fully converted into nitrogen-doped carbon material.

The above intermediate product (0.1073 g) was dispersed in 60 mL of ultrapure water. And 50 mg of $Na_2S{\cdot}9H_2O$ was dissolved in 40 mL of ultrapure water. Then, the two solutions were mixed quickly and the reaction was continued for 45 min under stirring. The black precipitate was collected by centrifugation and washed several times with water and absolute ethanol, and dried at 50 °C overnight. Afterward, the resulting black powder was etched in HNO_3 solution (1 M) for 12 h to remove the residual copper oxide in the product. The product was collected by centrifugation, washed, and dried to obtain the Cu_2S/Cu_7S_4/NC composites.

4.3. Characterizations. The morphology and structure of the synthesized samples were observed by a scanning electron microscope (SEM, JSM-7610F, Japan). The structure and composition of the product were confirmed by transmission electron microscopy (TEM, FEI Tecnai F30) with an X-ray energy-dispersive spectrometer (EDS). The phase and crystalline structures were examined by X-ray diffraction (XRD) measurement using a Bruker D8 advance (Germany) X-ray powder diffractometer. The composition and the chemical states of the elements were analyzed by X-ray photoelectron spectroscopy (XPS) on an ESCALAB 250Xi system (Thermo Fisher Scientific). N_2 adsorption−desorption measurements were conducted on a Trista II 3020 system (Micromeritics, America).

4.4. Electrochemical Measurements. The electrochemical properties of the samples were tested by CHI760E electrochemical workstation (Chenhua, China). The tests were performed in a three-electrode system, including the working electrode, the counter electrode (platinum plate electrode), and the reference electrode (Hg/HgO electrode). The electrolyte was a 2 M aqueous solution of potassium hydroxide. To ensure the accuracy and comparability of the electrochemical test results, all working electrodes were fabricated in exactly the same way. The specific preparation process of the working electrode was as follows: the prepared active material, acetylene black, and poly(tetrafluoroethylene) (PTFE) were evenly mixed with an 8:1:1 mass ratio in a small amount of ethanol. Then, the mixture was grounded and coated on the surface of a piece of pretreated nickel foam with an area of 1 cm × 1 cm. The nickel foam with active material was pressed and dried at 50 °C for 12 h.[57−59] To analyze the electrochemical behavior of the samples, cyclic voltammetry (CV), galvanostatic charge−discharge measurement (GCD), and electrochemical impedance spectroscopy (EIS) were performed. The specific capacitances were calculated according to the previous reports.[18,60−]

4.5. Fabrication of the Hybrid Supercapacitor. The practical application potential of the Cu_2S/Cu_7S_4/NC was further studied as the anode for hybrid supercapacitors. The activated carbon (AC) was used as the positive electrode, the synthesized Cu_2S/Cu_7S_4/NC was used as the negative electrode, and the 6 M KOH aqueous solution was employed as the electrolyte to construct the aqueous rechargeable device. The mass ratio of the positive electrode to the negative electrode was determined by the charge balance equations according to eqs 4 and 5.

$$q = C \times \Delta V \times m \tag{4}$$

$$\frac{m_+}{m_-} = \frac{C_- \times \Delta V_-}{C_+ \times \Delta V_+} \tag{5}$$

where m_+ and m_- (g) are the mass loading, C_+ and C_- ($F{\cdot}g^{-1}$) are the specific capacitance, and ΔV_+ and ΔV_- (V) are the applied potential of the positive and negative electrodes, respectively.

The energy density (E, $Wh{\cdot}kg^{-1}$) and the power density (P, $W{\cdot}kg^{-1}$) of the hybrid supercapacitor were determined based on eqs 6 and 7.

$$E = \frac{1}{2} C \Delta V^2 \tag{6}$$

$$P = \frac{E \times 3600}{\Delta t} \tag{7}$$

where C ($F{\cdot}g^{-1}$), ΔV (V), and Δt (s) are the specific capacitance, voltage, and the discharge time of the hybrid supercapacitor.

4.6. Computation Methods. The density functional theory (DFT) has been employed to perform the theoretical research using the DMol3 package. The projected augmented wave (PAW) was utilized to measure the ion−electron interactions. The spin-unrestricted DFT in the generalized gradient approximation with the Perdew−Burke−Ernzerhof (PBE) functional was applied. The cutoff energy for the plane-wave basis was 500 eV. Moreover, the vacuum was 15 Å to prevent the interactions among the periodic images along the z-direction. The Brillouin zone was sampled with the Monkhorst−Pack 3 × 4 × 1 and 7 × 9 × 1 k-point grids for geometry and electronic structure calculations, respectively. The energy and force convergence thresholds were set as 10^{-5} eV and 0.02 eV $Å^{-1}$ in the self-consistent field (SCF), respectively.

The adsorption energies for OH* and O* (ΔE_{OH} and ΔE_O) were calculated based on eqs 8 and 9.

$$\Delta E_{OH} = E_{total} - E_S - (E_{H_2O} - 1/2E_{H_2}) \tag{8}$$

$$\Delta E_O = E_{total} - E_S - (E_{H_2O} - E_{H_2}) \tag{9}$$

where E_{total} is the total energy of OH* or O* adsorbed on the materials, E_S is the total energy of the clean Cu_2O or Cu_2S without any adsorbates, and E_{H_2O} and E_{H_2} are the total energies of H_2O and H_2 free molecules in vacuum.

The Gibbs free energy (ΔG) was calculated based on eq 10.

https://doi.org/10.1021/acsomega.3c09627
ACS Omega 2024, 9, 11883−11894

$$\Delta G = \Delta E + \Delta \mathrm{ZPE} - T\Delta S \quad (10)$$

where ΔE is the calculated reaction energy, ΔZPE and $T\Delta S$ are the contributions of the zero-point energy and entropy to the ΔG.

■ ASSOCIATED CONTENT

Supporting Information

The Supporting Information is available free of charge at https://pubs.acs.org/doi/10.1021/acsomega.3c09627.

XRD pattern of Cu_2O; the theoretical calculation results; the other SEM images; the PDOS diagram of Cu_2S/Cu_7S_4/NC; and the CV and GCD comparisons of the Cu_2S/Cu_7S_4/NC products prepared with different dosages of $Na_2S{\cdot}9H_2O$ (PDF)

■ AUTHOR INFORMATION

Corresponding Authors

Liu Yang − *School of Chemical Engineering, Northeast Electric Power University, Jilin 132012, P. R. China;* orcid.org/0000-0002-3635-8472; Email: l.yang@neepu.edu.cn

Xiaohui Guan − *School of Chemical Engineering, Northeast Electric Power University, Jilin 132012, P. R. China;* orcid.org/0000-0003-1490-0766; Email: guanxh@neepu.edu.cn

Authors

Yu Yin − *CHN Energy Zhejiang Electric Power Co., Ltd., Hangzhou, Zhejiang 310000, P. R. China*

Shuo Zhang − *CHN Energy Zhejiang Electric Power Co., Ltd., Hangzhou, Zhejiang 310000, P. R. China*

Yaoxuan Liu − *China Energy Science and Technology Research Institute Co.,Ltd., Nanjing 210000, P. R. China*

Zunyun Huang − *CHN Energy Zhejiang Electric Power Co., Ltd., Hangzhou, Zhejiang 310000, P. R. China*

Wenbin Sun − *CHN Energy Zhejiang Electric Power Co., Ltd., Hangzhou, Zhejiang 310000, P. R. China*

Mingze Zhang − *CHN Energy Zhejiang Electric Power Co., Ltd., Hangzhou, Zhejiang 310000, P. R. China*

Enzhen Zhou − *CHN Energy Zhejiang Electric Power Co., Ltd., Hangzhou, Zhejiang 310000, P. R. China*

Haihui Wu − *School of Chemical Engineering, Northeast Electric Power University, Jilin 132012, P. R. China*

Penggang Yin − *School of Chemistry, Beihang University, Beijing 100191, P. R. China;* orcid.org/0000-0001-6796-5921

Complete contact information is available at: https://pubs.acs.org/10.1021/acsomega.3c09627

Notes

The authors declare no competing financial interest.

■ ACKNOWLEDGMENTS

The authors acknowledge the funding support from the National Natural Science Foundation of China (51972049, 52202217).

■ REFERENCES

(1) Gan, Z.; Yin, J.; Xu, X.; Cheng, Y.; Yu, T. Nanostructure and Advanced Energy Storage: Elaborate Material Designs Lead to High-Rate Pseudocapacitive Ion Storage. *ACS Nano* **2022**, *16*, 5131−5152.

(2) Zhao, H.; Lei, Y. 3D Nanostructures for the Next Generation of High-Performance Nanodevices for Electrochemical Energy Conversion and Storage. *Adv. Energy Mater.* **2020**, *10*, No. 2001460.

(3) Wang, C.; Zhao, S.; Song, X.; Wang, N.; Peng, H.; Su, J.; Zeng, S.; Xu, X.; Yang, J. Suppressed Dissolution and Enhanced Desolvation in Core−Shell MoO_3@TiO_2 Nanorods as a High-Rate and Long-Life Anode Material for Proton Batteries. *Adv. Energy Mater.* **2022**, *12*, No. 2200157, DOI: 10.1002/aenm.202200157.

(4) Liu, Y.; Wu, X. High durable aqueous zinc ion batteries by synergistic effect of V_6O_{13}/VO_2 electrode materials. *J. Mater. Chem.* **2023**, *87*, 334−341.

(5) Xie, K.; Zhang, W.; Ren, K.; Zhu, E.; Lu, J.; Chen, J.; Yin, P.; Yang, L.; Guan, X.; Wang, G. Electrochemical performance of corn waste derived carbon electrodes based on the intrinsic biomass properties. *Materials* **2023**, *16*, No. 5022, DOI: 10.3390/ma16145022.

(6) Yang, L.; Lu, X.; Wang, S.; Wang, J.; Guan, X.; Guan, X.; Wang, G. Designed synthesis of nickel−cobalt-based electrode materials for high-performance solid-state hybrid supercapacitors. *Nanoscale* **2020**, *12*, 1921−1938.

(7) An, C.; Wu, S.; Gao, L.; Lin, L.; Deng, Q.; Hu, N. Core-shell NiS_2@C encased by thin carbon layer as high-rate and durable electrode for aqueous rechargeable battery. *J. Colloid Interface Sci.* **2023**, *638*, 274−280.

(8) Ikezawa, A.; Koyama, Y.; Nishizawa, T.; Arai, H. A high voltage aqueous proton battery using an optimized operation of a MoO_3 positive electrode. *J. Mater. Chem. A* **2023**, *11*, 2360−2366.

(9) Niu, L.; Wu, T.; Chen, M.; Yang, L.; Yang, J.; Wang, Z.; Kornyshev, A. A.; Jiang, H.; Bi, S.; Feng, G. Conductive Metal-Organic Frameworks for Supercapacitors. *Adv. Mater.* **2022**, *34*, No. 2200999.

(10) Zhang, H.; Yang, D.; Lau, A.; Ma, T.; Lin, H.; Jia, B. Hybridized Graphene for Supercapacitors: Beyond the Limitation of Pure Graphene. *Small* **2021**, *17*, No. 2007311.

(11) Zhang, M.; Hu, T.; Chang, P.; Jin, Z.; Mei, H.; Dong, N.; Cheng, L. 3D printing of CuO/Cu@Mullite electrodes with macroporous structures and their strong regulation on zinc ion storage. *Ceram. Int.* **2022**, *48*, 4124−4133.

(12) Yu, X.; Hu, F.; Guo, Z.-Q.; Liu, L.; Song, G.-H.; Zhu, K. High-performance $Cu_{0.95}V_2O_5$ nanoflowers as cathode materials for aqueous zinc-ion batteries. *Rare Met.* **2022**, *41*, 29−36.

(13) Liu, Y.; Li, Q.; Ma, K.; Yang, G.; Wang, C. Graphene oxide wrapped CuV_2O_6 nanobelts as high-capacity and long-life cathode materials of aqueous zinc-ion batteries. *ACS Nano* **2019**, *13*, 12081−12089.

(14) Wang, X.; Zhang, M.; Mei, H.; Chang, P.; Cheng, L. Ultra-pressure-resistant SiOC@Cu_2Se 3D printed cathode for aqueous zinc-ion batteries. *Ceram. Int.* **2021**, *47*, 24699−24706.

(15) Fenta, F. W.; Olbasa, B. W.; Tsai, M.-C.; Weret, M. A.; Zegeye, T. A.; Huang, C.-J.; Huang, W.-H.; Zeleke, T. S.; Sahalie, N. A.; Pao, C.-W.; et al. Electrochemical transformation reaction of Cu−MnO in aqueous rechargeable zinc-ion batteries for high performance and long cycle life. *J. Mater. Chem. A* **2020**, *8*, 17595−17607.

(16) Wu, J.; Meng, J.; Yang, Z.; Chen, H.; Rong, Y.; Deng, L.; Fu, Z. Energy storage mechanism and electrochemical performance of Cu_2O/rGO as advanced cathode for aqueous zinc ion batteries. *J. Alloys Compd.* **2022**, *895*, No. 162653.

(17) Amirtharaj, S. N.; Mariappan, M. A facile synthesis of interconnected CuO nanosheets: a promising electrode material for supercapacitor application. *Appl. Phys. A* **2021**, *127*, No. 511, DOI: 10.1007/s00339-021-04649-9.

(18) Barqi, J.; Masoudpanah, S.; Liu, X.; Bafghi, M. S.; Ong, C. Fabrication of porous Cu_2S nanosheets for high performance hybrid supercapacitor. *J. Energy Storage* **2022**, *45*, No. 103781.

(19) Ranjith Kumar, D.; Kesavan, S.; Baynosa, M. L.; Shim, J.-J. Flower-like $Cu_{1.8}S$ nanostructures for high-performance flexible solid-state supercapacitors. *Appl. Surf. Sci.* **2018**, *448*, 547−558.

(20) Ning, J.; Zhang, T.; He, Y.; Jia, C.; Saha, P.; Cheng, Q. Co_3O_4@CoS core-shell nanosheets on carbon cloth for high

performance supercapacitor electrodes. *Materials* **2017**, *10*, No. 608, DOI: 10.3390/ma10060608.
(21) Peng, H.; Ma, G.; Sun, K.; Mu, J.; Wang, H.; Lei, Z. High-performance supercapacitor based on multi-structural CuS@polypyrrole composites prepared by in situ oxidative polymerization. *J. Mater. Chem. A* **2014**, *2*, 3303−3307.
(22) Li, J.; Sun, L.; Yan, Y.; Zhu, Z. A novel fabrication of Cu_2O@Cu_7S_4 core-shell micro/nanocrystals from Cu_2O temples and enhanced photocatalytic activities. *Mater. Res. Bull.* **2016**, *80*, 200−208.
(23) Ivanchenko, M.; Carroll, A. L.; Brothers, A. B.; Jing, H. Facile aqueous synthesis of hollow dual plasmonic hetero-nanostructures with tunable optical responses through nanoscale Kirkendall effects. *Nanoscale Adv.* **2022**, *5*, 88−95.
(24) Zhang, X.; Li, X.; Liang, J.; Zhu, Y.; Qian, Y. Synthesis of MoS_2@C Nanotubes Via the Kirkendall Effect with Enhanced Electrochemical Performance for Lithium Ion and Sodium Ion Batteries. *Small* **2016**, *12*, 2484−2491.
(25) Dong, Y.; Zhang, X.; Wang, X.; Liu, F.; Ren, J.; Wang, H.; Wang, R. Kirkendall effect Strengthened-Superhydrophilic/superaerophobic Co-Ni_3N/NF heterostructure as electrode catalyst for High-current hydrogen production. *J. Colloid Interface Sci.* **2023**, *636*, 657−667.
(26) Ling, X.; Wei, W.; Shan, C.; Qin, X.; Song, M.; Liu, Z.; Mi, L. Ball-in-ball NiS^2@CoS^2 heterojunction driven by Kirkendall effect for high-performance Mg^{2+}/Li^+ hybrid batteries. *J. Colloid Interface Sci.* **2024**, *658*, 688−698.
(27) Rasappan, A. S.; Thangamuthu, V.; Natarajan, M.; Velauthapillai, D. Kirkendall effect induced NiFe: WS_2 core-shell nanocubes for Dye-sensitized solar cell and battery-type Supercapacitor applications. *J. Energy Storage* **2023**, *63*, No. 106964, DOI: 10.1016/j.est.2023.106964.
(28) Jin, L.; You, S.; Yao, Y.; Chen, H.; Wang, Y.; Liu, Y. An electroactive single-atom copper anchored MXene nanohybrid filter for ultrafast water decontamination. *J. Mater. Chem. A* **2021**, *9*, 25964−25973.
(29) Madkour, M. Cu_xO thin films via ultrasonic spray pyrolysis as efficient solar photocatalysts: Single source polymeric coordinated precursor. *Colloid Interface Sci. Commun.* **2021**, *44*, No. 100497.
(30) Peng, Q.; Zhang, S.; Yang, H.; Sheng, B.; Xu, R.; Wang, Q.; Yu, Y. Boosting potassium storage performance of the Cu_2S anode via morphology engineering and electrolyte chemistry. *ACS Nano* **2020**, *14*, 6024−6033.
(31) Jia, Z.; Wang, Y.; Chen, J.; Cao, Z.; Pan, S.; Zhou, Y.; Sun, J.; Zhu, J.; Wang, X.; Fu, Y. Metal-organic frameworks derived low-crystalline $NiCo_2S_4$/Co_3S_4 nanocages with dual heterogeneous interfaces for high-performance supercapacitors. *Chin. Chem. Lett.* **2023**, *34*, No. 107137.
(32) Pataniya, P. M.; Patel, V.; Sahatiya, P.; Late, D. J.; Sumesh, C. Hydrogen evolution reaction in acidic and basic medium on robust cobalt sulphide electrocatalyst. *Surf. Interfaces* **2022**, *34*, No. 102319.
(33) Chen, H.; Zhan, J.; Man, L.; Deng, H.; Zhou, H.; Hao, L.; Zhou, X. High foliar retention tannic acid/Fe^{3+} functionalized Ti-pillared montmorillonite pesticide formulation with pH-responsibility and high UV stability. *Appl. Surf. Sci.* **2023**, *620*, No. 156838.
(34) Li, Y.; Qiao, L.; Yin, S.; Cheng, X.; Wang, C.-T.; Jiang, Y.; Sun, S. A plasma-assisted approach to enhance density of accessible FeN_4 sites for proton exchange membrane fuel cells. *J. Colloid Interface Sci.* **2023**, *647*, 224−232.
(35) Liu, Y.; Wang, H.; Li, C.; Wang, S.; Li, L.; Song, C.; Wang, T. Hierarchical flaky porous carbon derived from waste polyimide film for high-performance aqueous supercapacitor electrodes. *Int. J. Energy Res.* **2022**, *46*, 370−382.
(36) Ren, G.; Li, Y.; Chen, Q.; Qian, Y.; Zheng, J.; Zhu, Y.; Teng, C. Sepia-derived N, P Co-doped porous carbon spheres as oxygen reduction reaction electrocatalyst and supercapacitor. *ACS Sustainable Chem. Eng.* **2018**, *6*, 16032−16038.
(37) Zhu, T.; Ding, J.; Shao, Q.; Qian, Y.; Huang, X. P, Se-Codoped MoS_2 Nanosheets as Accelerated Electrocatalysts for Hydrogen Evolution. *ChemCatChem* **2019**, *11*, 689−692.
(38) Chen, J.; Lin, C.; Zhang, M.; Jin, T.; Qian, Y. Constructing Nitrogen, Selenium Co-Doped Graphene Aerogel Electrode Materials for Synergistically Enhanced Capacitive Performance. *ChemElectroChem* **2020**, *7*, 3311−3318.
(39) Zou, J.; Xie, D.; Xu, J.; Song, X.; Zeng, X.; Wang, H.; Zhao, F. Rational design of honeycomb Ni-Co LDH/graphene composite for remarkable supercapacitor via ultrafast microwave synthesis. *Appl. Surf. Sci.* **2022**, *571*, No. 151322.
(40) Wu, K.; Li, H.; Liang, S.; Ma, Y.; Yang, J. Phenazine-based Compound Realizing Separate Hydrogen and Oxygen Production in Electrolytic Water Splitting. *Angew. Chem., Int. Ed.* **2023**, *62*, No. e202303563.
(41) Zhang, R.; Dong, J.; Zhang, W.; Ma, L.; Jiang, Z.; Wang, J.; Huang, Y. Synergistically coupling of 3D FeNi-LDH arrays with Ti_3C_2Tx-MXene nanosheets toward superior symmetric supercapacitor. *Nano Energy* **2022**, *91*, No. 106633.
(42) Li, S.; Luo, Y.; Wang, C.; Wu, M.; Xue, Y.; Yang, J.; Li, L. A novel hierarchical core-shell structure of $NiCo_2O_4$@NiCo-LDH nanoarrays for higher-performance flexible all-solid-state supercapacitor electrode materials. *J. Alloys Compd.* **2022**, *920*, No. 165986.
(43) Das, A. K.; Pan, U. N.; Sharma, V.; Kim, N. H.; Lee, J. H. Nanostructured CeO_2/NiV−LDH composite for energy storage in asymmetric supercapacitor and as methanol oxidation electrocatalyst. *Chem. Eng. J.* **2021**, *417*, No. 128019.
(44) Yang, L.; Wang, J.; Wang, S.; Guan, X.; Guan, X.; Wang, G. Biomass-derived multi-heteroatom-doped carbon materials for high-performance solid-state symmetric supercapacitors with superior long-term cycling stability. *Ionics* **2020**, *26*, 4141−4151.
(45) Ma, F.; Ma, D.; Wu, G.; Geng, W.; Shao, J.; Song, S.; Wan, J.; Qiu, J. Construction of 3D nanostructure hierarchical porous graphitic carbons by charge-induced self-assembly and nanocrystal-assisted catalytic graphitization for supercapacitors. *Chem. Commun.* **2016**, *52*, 6673−6676.
(46) Ma, C.; Li, Y.; Shi, J.; Song, Y.; Liu, L. High-performance supercapacitor electrodes based on porous flexible carbon nanofiber paper treated by surface chemical etching. *Chem. Eng. J.* **2014**, *249*, 216−225.
(47) Wang, S.; Pei, B.; Zhao, X.; Dryfe, R. A. Highly porous graphene on carbon cloth as advanced electrodes for flexible all-solid-state supercapacitors. *Nano Energy* **2013**, *2*, 530−536.
(48) Li, Z.; Wu, D.; Liang, Y.; Fu, R.; Matyjaszewski, K. Synthesis of well-defined microporous carbons by molecular-scale templating with polyhedral oligomeric silsesquioxane moieties. *J. Am. Chem. Soc.* **2014**, *136*, 4805−4808.
(49) Gao, D.; Wang, L.; Yu, J.; Wei, Q.; Wang, C.; Liu, G. Preparation and characterization of porous carbon based nanocomposite for supercapacitor. *Fibers Polym.* **2014**, *15*, 1236−1241.
(50) Liu, B.; Yang, M.; Chen, H.; Liu, Y.; Yang, D.; Li, H. Graphene-like porous carbon nanosheets derived from salvia splendens for high-rate performance supercapacitors. *J. Power Sources* **2018**, *397*, 1−10.
(51) Le, T.; Yang, Y.; Huang, Z.; Kang, F. Preparation of microporous carbon nanofibers from polyimide by using polyvinyl pyrrolidone as template and their capacitive performance. *J. Power Sources* **2015**, *278*, 683−692.
(52) He, X.; Li, R.; Qiu, J.; Xie, K.; Ling, P.; Yu, M.; Zhang, X.; Zheng, M. Synthesis of mesoporous carbons for supercapacitors from coal tar pitch by coupling microwave-assisted KOH activation with a MgO template. *Carbon* **2012**, *50*, 4911−4921.
(53) Lai, C.; Zhou, Z.; Zhang, L.; Wang, X.; Zhou, Q.; Zhao, Y.; Wang, Y.; Wu, X.-F.; Zhu, Z.; Fong, H. Free-standing and mechanically flexible mats consisting of electrospun carbon nanofibers made from a natural product of alkali lignin as binder-free electrodes for high-performance supercapacitors. *J. Power Sources* **2014**, *247*, 134−141.
(54) Chen, L.-F.; Zhang, X.-D.; Liang, H.-W.; Kong, M.; Guan, Q.-F.; Chen, P.; Wu, Z.-Y.; Yu, S.-H. Synthesis of nitrogen-doped porous

carbon nanofibers as an efficient electrode material for supercapacitors. *ACS Nano* **2012**, *6*, 7092−7102.
(55) Luo, L.; Lan, Y.; Zhang, Q.; Deng, J.; Zeng, Q.; Gao, H.; Du, G.; Zhao, W. Enhanced capacitance of phosphorus, nitrogen, and oxygen tri-doped balsa wood-based porous carbon for supercapacitors. *J. Energy Storage* **2023**, *58*, No. 106339, DOI: 10.1016/j.est.2022.106339.
(56) Fang, Y.; Luan, D.; Chen, Y.; Gao, S.; Lou, X. W. Rationally designed three-layered Cu_2S@Carbon@MoS_2 hierarchical nanoboxes for efficient sodium storage. *Angew. Chem.* **2020**, *132*, 7245−7250.
(57) Guan, X.; Chen, J.; Zhu, E.; Yin, P.; Yang, L.; Guan, X.; Wang, G. Intrinsic electrochemical activity modulation of MOF-derived C/N-NiCoMn-LDH/Ag electrode for low temperature hybrid supercapacitors. *J. Mater. Sci. Technol.* **2023**, *150*, 145−158.
(58) Wang, J.; Yang, L.; Fu, Y.; Yin, P.; Guan, X.; Wang, G. Delicate control of crystallographic Cu_2O derived Ni−Co amorphous double hydroxide nanocages for high-performance hybrid supercapacitors: an experimental and computational investigation. *Nanoscale* **2021**, *13*, 8562−8574.
(59) Yang, L.; Huang, M.; Lu, M.; Guan, X.; Guan, X.; Wang, G.; Jia, B. Facile design and synthesis of nickle-molybdenum oxide/sulfide composites with robust microsphere structure for high-performance supercapacitors. *Chem. Eng. J.* **2019**, *364*, 462−474.
(60) Noori, A.; El-Kady, M. F.; Rahmanifar, M. S.; Kaner, R. B.; Mousavi, M. F. Towards establishing standard performance metrics for batteries, supercapacitors and beyond. *Chem. Soc. Rev.* **2019**, *48*, 1272−1341.
(61) Mathis, T. S.; Kurra, N.; Wang, X.; Pinto, D.; Simon, P.; Gogotsi, Y. Energy storage data reporting in perspective—guidelines for interpreting the performance of electrochemical energy storage systems. *Adv. Energy Mater.* **2019**, *9*, No. 1902007.
(62) Han, X.; Zhang, D.; Qin, Y.; Kong, X.; Zhang, F.; Lei, X. Construction of Ta-Cu_7S_4 negative electrode for high-performance all-solid-state asymmetric supercapacitor. *Chem. Eng. J.* **2021**, *403*, No. 126471.

https://doi.org/10.1021/acsomega.3c09627
ACS Omega 2024, 9, 11883−11894